

# Linear-Model-inspired Neural Network for Electromagnetic Inverse Scattering

Huilin Zhou<sup>1\*</sup>, Yadan Li<sup>1</sup>, Tao Ouyang<sup>1</sup>, Jian Liu<sup>1</sup>, Qiegen Liu<sup>1</sup>, Senior Member, IEEE

<sup>1</sup>Department of Electronic Information Engineering, Nanchang University, Nanchang, 330031, China

**Abstract**—Electromagnetic inverse scattering problems (ISPs) aim to retrieve permittivities of dielectric scatterers from the scattering measurement. It is often highly non-linear, causing the problem to be very difficult to solve. To alleviate the issue, this letter exploits a linear model-based network (LMN) learning strategy, which benefits from both model complexity and data learning. By introducing a linear model for ISPs, a new model with network-driven regularizer is proposed. For attaining efficient end-to-end learning, the network architecture and hyper-parameter estimation are presented. Experimental results validate its superiority to some state-of-the-arts.

**Index Terms**—Electromagnetic inverse scattering, linear model, deep learning, network-driven regularizer

## 1. INTRODUCTION

ELECTROMAGNETIC inverse scattering problems (ISPs) are devoted to reconstructing the location, shape, and some electrical properties of unknown objects from the measured scattered fields. The desired objects are located inside a bounded domain of interest (DoI) immersed in a known background medium. ISPs have been attracting attentions for many years and have various applications [1-6], such as nondestructive testing, through-wall imaging, geophysics, and remote sensing. They can be roughly described by Lippmann–Schwinger equation for the field inside and outside the scattering object. It is challenging to address due to the intrinsically ill-posed and non-linear property.

Related solutions for ISPs have been vigorously presented, which can be divided into linear and non-linear methods. In the category of linear method, it is assumed that the difference between the incident field and the total field is less than 30%, and thus the first-order Born approximation (BA) is used to describe the total field [7]. In this circumstance, the total field inside the medium with the incident field can be replaced by ignoring the multiple scattering effect between the target and the medium, thereby linearizing the target contrast and receiving that related to the scattering field [8]. Additionally, many regularization methods were proposed to alleviate the ill-posed deficiency, including the truncated singular value decomposition (TSVD) [9] and low rank constraint [10]. In summary, these methods have higher parameter inversion

speed and accuracy in the case of the medium target to be a weak scatterer, i.e., the difference between the dielectric constant of the target and the background is small or the target size is not much larger than the wavelength of the incident electromagnetic wave. Nonetheless, they are not suitable for strong scatterers.

The category of nonlinear method assumes that the multiple scattering effects are caused by the interaction of the incident wave with medium target. The total field in the imaging region is the superposition of the incident field and the scattering field. Due to the inherent non-linearity and ill-posedness of ISPs, regularization-induced iterative optimization methods are put forward, like contrast source-type inversion (CSI) [13–14], Born iterative method and its variants [11-12], and subspace optimization method (SOM) [15–16]. The benefit of iterative strategy is that the formula is rigorous and can reconstruct the spatial distribution of strong scatterers. Nevertheless, it is often sensitive to initial values and converges in relatively slow speed. It also needs to manually set the iteration number and regularization parameters.

Recently, deep learning has gained promising performance in various engineering applications. Although employing deep learning scheme directly may attain outstanding results, it fails to integrate with the physical knowledge that is related to electromagnetic inverse scattering [17-21]. Very recently, there is a work that tries to incorporate the physic scheme into the network design, while it is designed to nonlinear model [22]. In this letter, we propose a scheme based on convolutional neural networks (CNN) to tackle ISPs with linear constraint [23]. The learnable network consists of a set of alternative CNN denoiser sub-network and data-fidelity sub-network.

## 2. LMN: LINEAR MODEL-BASED NETWORK

### 2.1. Linear Model for ISPs

A two-dimensional (2D) transverse magnetic (TM, i.e. Ez polarization) ISPs is shown in Fig. 1. The unknown nonmagnetic scatterers are within a free-space background DOI ( $D \subset R^2$ ). They are illuminated by incoming electromagnetic waves, which are generated by transmitters located at  $r_j$ ,  $j = 1, 2, \dots, N_j$ . For each incidence, the scattered field is measured by an array of receivers that located at  $r_q$ ,  $q = 1, 2, \dots, N_s$ .

The forward formulation of ISPs can be described by two equations. Specifically, the first one is the Lippmann–Schwinger equation, or equivalent domain integral equation:

H. Zhou, Y. Li, T. Ouyang, J. Liu and Q. Liu are with the Department of Electronic Information Engineering, Nanchang University, 330031, China. ({416114417145, liujian}@email.ncu.edu.cn, m18702609359@163.com, {zhouhuilin, liuqiegen}@ncu.edu.cn).

$$\bar{\bar{E}}_{\text{tot}} = \bar{\bar{E}}_{\text{inc}} + \bar{\bar{G}}_D \bar{\bar{\chi}} \bar{\bar{E}}_{\text{tot}} \quad (1)$$

where  $\bar{\bar{E}}_{\text{inc}}$  and  $\bar{\bar{E}}_{\text{tot}}$  denote the incident and total electric fields, respectively. The diagonal matrix  $\bar{\bar{\chi}}$  denotes the contrast of reconstructed object scatterer whose diagonal element is  $\bar{\bar{\chi}}(n, n) = \varepsilon_r(r_n) - 1$ ,  $\varepsilon_r(r_n)$  is the relative permittivity at  $r_n$ .  $\bar{\bar{G}}_D$  is a 2D free space Green's function in domain  $D$ .

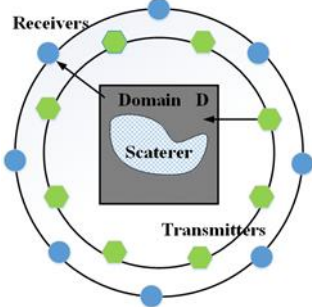


Fig. 1. Schematic diagram of inverse scattering problems.

The discretized formulation of the second equation in ISPs is

$$\bar{\bar{E}}_{\text{sca}} = \bar{\bar{G}}_S \bar{\bar{\chi}} \bar{\bar{E}}_{\text{tot}} \quad (2)$$

where  $\bar{\bar{E}}_{\text{sca}}$  is the scattered field.  $\bar{\bar{G}}_S$  is a 2D free space Green's function in domain  $S$ .

The pursuit of inverse scattering problem is to determine the relative permittivities of the scatterer from the observed scattered field  $\bar{\bar{E}}_{\text{sca}}$  via Eqs. (1)(2). At a first glance, it is a non-linear equation. However, as discussed in Introduction section, in some special case, ISPs can be solved by BA [7]. i.e.,

$$\bar{\bar{E}}_{\text{sca}} = \bar{\bar{G}}_S \bar{\bar{\chi}} \bar{\bar{E}}_{\text{inc}} \quad (3)$$

By rewriting the element-wise multiplication in the matrix formulation, it yields

$$\bar{\bar{E}}_{\text{sca}} = \bar{\bar{G}}_S \text{diag}(\bar{\bar{E}}_{\text{inc}}) \bar{\bar{\chi}} \quad (4)$$

By introducing regularization term into the linear model, there exists

$$\bar{\bar{\chi}} = \arg \min_{\bar{\bar{\chi}}} \left\| \bar{\bar{E}}_{\text{sca}} - \bar{\bar{G}}_S \text{diag}(\bar{\bar{E}}_{\text{inc}}) \bar{\bar{\chi}} \right\|_2^2 + \lambda \|R_w(\bar{\bar{\chi}})\|^2 \quad (5)$$

where  $R_w(\bar{\bar{\chi}})$  is a learnable CNN estimator that depends on the network parameters  $w$ .

## 2.2. Network Architecture of LMN

By setting  $R_w(\bar{\bar{\chi}})$  to be network-contained, it yields,

$$R_w(\bar{\bar{\chi}}) = \bar{\bar{\chi}} - V_w(\bar{\bar{\chi}}) \quad (6)$$

where  $V_w(\bar{\bar{\chi}})$  is the desired clean version of  $\bar{\bar{\chi}}$ , after the removal of distorted signals. The CNN-based prior  $\|R_w(\bar{\bar{\chi}})\|^2$  tries to avoid signal corruption as well as guarantee data-consistency. Substituting Eq. (6) into Eq. (5), it attains:

$$\bar{\bar{\chi}}_{\text{rec}} = \arg \min_{\bar{\bar{\chi}}} \left\| \bar{\bar{E}}_{\text{sca}} - \bar{\bar{G}}_S \text{diag}(\bar{\bar{E}}_{\text{tot}}) \bar{\bar{\chi}} \right\|_2^2 + \lambda \|\bar{\bar{\chi}} - V_w(\bar{\bar{\chi}})\|^2 \quad (7)$$

By introducing auxiliary intermediate variable  $Z$ , we obtain an alternating iterative formulation that approximates to Eq. (7):

$$\bar{\bar{\chi}}_{n+1} = \arg \min_{\bar{\bar{\chi}}} \left\| \bar{\bar{E}}_{\text{sca}} - \bar{\bar{G}}_S \text{diag}(\bar{\bar{E}}_{\text{tot}}) \bar{\bar{\chi}} \right\|_2^2 + \lambda \|\bar{\bar{\chi}} - Z_n\|^2 \quad (8a)$$

$$Z_{n+1} = V_w(\bar{\bar{\chi}}_{n+1}) \quad (8b)$$

By calculating the gradient of sub-problem Eq. (8a) and letting it to be zero, it attains:

$$[(\bar{\bar{G}}_S \text{diag}(\bar{\bar{E}}_{\text{tot}}))^H (\bar{\bar{G}}_S \text{diag}(\bar{\bar{E}}_{\text{tot}})) + \lambda I] \bar{\bar{\chi}}_{n+1} = (\bar{\bar{G}}_S \text{diag}(\bar{\bar{E}}_{\text{tot}}))^H (\bar{\bar{E}}_{\text{sca}}) + \lambda Z_n \quad (9)$$

The schematic diagram of the iterative framework is shown in Fig. 2, where  $A = \bar{\bar{G}}_S \text{diag}(\bar{\bar{E}}_{\text{tot}})$ . After initializing with  $\bar{\bar{\chi}}_0 = A^H \bar{\bar{E}}_{\text{sca}}$ , it alternatively updates  $Z_n$  and  $\bar{\bar{\chi}}_{n+1}$  by CNN-based denoiser step Eq. (8b) and conjugate gradient step Eq. (9).

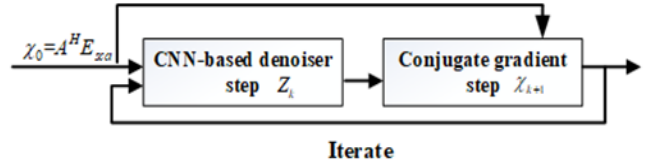


Fig. 2. An illustration of the iteration scheme in Eq. (8b) and Eq. (9).

By regarding one iteration as one layer, the above update rule can be viewed as an unrolled deep CNN, whose weights at different iterations are shared. An end-to-end training scheme is employed to optimize it. The proposed unrolled architecture uses the same denoising operator  $V_w(\bar{\bar{\chi}})$  at each layer, hence significant reduction in model complexity is allowed. Besides,  $\lambda$  is a trainable regularization parameter. High  $\lambda$ -value in the training procedure indicates that the constrained setting can achieve improvement.

In summary, the flowchart of network LMN is depicted in Fig. 3, which consists of a series of learnable CNN denoiser sub-network and data-consistency (DC) sub-network. Specifically, the widely used residual network is adopted in the CNN denoiser sub-network. At the meantime, conjugate gradient is done in the DC sub-network.

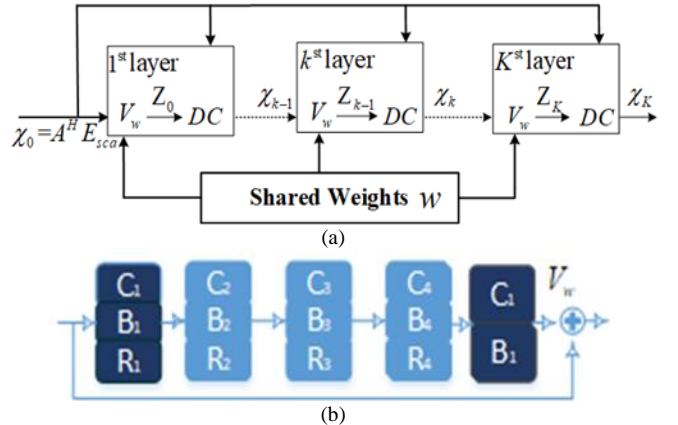


Fig. 3. The flowchart of the LMN network (a) and the CNN denoiser sub-network (b). Here the Conv, BN and ReLU layers are denoted as ‘‘C’’, ‘‘B’’ and ‘‘R’’, respectively.

## 2.3. Parameter Solver of LMN

As seen in the previous subsection, decoupling the training process from the specifics of the acquisition procedure simplifies the approach. Besides of the network architecture, we

leverage the performance of the network via directly minimizing the loss function by means of end-to-end fashion. i.e., assuming the number of layer to be  $K$ , the loss function between  $\bar{\bar{\chi}}_K$  and the desired image  $\hat{\chi}$  is defined as follows:

$$L = \sum_{i=1}^{N_{samples}} \left\| \bar{\bar{\chi}}_K(i) - \hat{\chi}(i) \right\|^2 \quad (10)$$

where  $\hat{\chi}(i)$  is the  $i$ -th label image. By means of minimizing Eq. (10), the parameters in CNN sub-network and DC sub-network will be updated via training on data pairs.

At first, the gradient of the cost function Eq. (10) with respect to the shared weights  $w$  is given by the chain rule

$$(\nabla_w L) = \sum_{k=0}^{K-1} J_w(\mathbf{Z}_k)^T (\nabla_{\mathbf{Z}_k} L) \quad (11)$$

where the element of the Jacobian matrix  $J_w(\mathbf{Z})$  is  $[J_w(\mathbf{Z})]_{i,j} = \partial z_i / \partial w_j$  and  $z_k$  is the output of CNN at  $k$ -th layer.

In order to apply the backpropagation scheme to Eq. (11), the next step is how to evaluate the terms  $\nabla_{\mathbf{Z}_k} L, k = 0, \dots, K-1$ .

According to the formulation of Eq. (9), we backpropagate them via designing numerical optimization blocks, i.e., conjugate gradient (CG) blocks [24]. Concretely, according to the chain rule, it has

$$\nabla_{\mathbf{Z}_{k-1}} L = J_{\mathbf{Z}_{k-1}}(\bar{\bar{\chi}}_k)^T \nabla_{\bar{\bar{\chi}}_k} L \quad (12)$$

where the Jacobian matrix  $J_{\mathbf{Z}}(\bar{\bar{\chi}})$  has entries  $[J_{\mathbf{Z}}(\bar{\bar{\chi}})]_{i,j} = \partial x_i / \partial z_j$ . By calculating the gradient from Eq. (9), the value of Jacobian matrix is given by

$$J_{\mathbf{Z}}(\bar{\bar{\chi}}) = [(\bar{\bar{\mathbf{G}}}_s \text{diag}(\bar{\bar{\mathbf{E}}}_{\text{tot}}))^H (\bar{\bar{\mathbf{G}}}_s \text{diag}(\bar{\bar{\mathbf{E}}}_{\text{tot}})) + \lambda I]^{-1} \quad (13)$$

Finally, after Eq. (12) is determined, the network parameter of the network  $V_w$  and the regularization parameter  $\lambda$  can also be updated by Adam optimization scheme [25].

### 3. EXPERIMENTAL RESULTS

The performance of proposed network LMN is evaluated in reconstructing relative permittivities from scattered field. We implemented its architecture in MATLAB on a PC equipped with Inter(R) Core (TM) i7-7800X CPU and GeForce Titan 1080Ti. Results under synthetic data including circular-cylinder and MNIST datasets [26] are presented.

#### 3.1. Experiment Configuration

In the experiment, a domain of interest(DOI) with size of  $2 \times 2 \text{ m}^2$  is divided into  $128 \times 128$  pixels. In the inversion process, in order to avoid the inverse crisis, the DoI is divided into  $30 \times 30$  and  $64 \times 64$  pixels, respectively. Among yhem, 16 line sources and 32 line receivers are equally placed on a circle centered at  $(0, 0) \text{ m}$  and with diameter 12 m and 6 m. The scattered fields are generated numerically using the method of moment (MOM) and recorded into  $\bar{\bar{\mathbf{E}}}_{\text{sca}}$ , which is a matrix with  $N_r \times N_i$  dimensions. By inserting additive white Gaussian noise  $\bar{\bar{n}}$ , the measured scattered field  $\bar{\bar{\mathbf{E}}}_{\text{sca}} + \bar{\bar{n}}$  is utilized to reconstruct relative permittivities. The noise level is relatively defined as  $\|\bar{\bar{n}}\|_F / \|\bar{\bar{\mathbf{E}}}_{\text{sca}}\|_F$ . The operating frequency is 400 MHz, and a

priori information is that the scatterers are lossless as well as fall into the range of nonnegative contrast [13].

In order to evaluate the reconstruction performance of these algorithms, a relative error of the reconstructed permittivity  $R_e$  is defined as

$$R_e = \frac{1}{M_t} \sum_{j=1}^{M_t} \left\| \bar{\bar{\epsilon}}_r^t - \bar{\bar{\epsilon}}_r^r \right\|_F / \left\| \bar{\bar{\epsilon}}_r^t \right\|_F \quad (14)$$

where  $\bar{\bar{\epsilon}}_r^r$  and  $\bar{\bar{\epsilon}}_r^t$  are the reconstructed relative permittivity and ground-truth relative permittivity.  $M_t$  is the number of conducted tests.

#### 3.2. Algorithm Robustness

In order to investigate the generalization feasibility of the introduced LMN, we thoroughly evaluate the network trained under MNIST dataset [26], which consists of various handwriting Latin letters that used in machine learning community. The number of handwritten digits is 70 000, and each one has a size of  $28 \times 28$  pixels. Rather than recognizing and classifying the Latin letters, we quantitatively reconstruct the profile where the scatterers are represented by the Latin letters. To this end, the relative permittivity in the training data is a special value. At the meantime, the relative permittivity of the testing letters belongs to the interval of 1.5-2.4. In the example, the 100 images and 25 images are utilized to presented in training and testing procedure, respectively.

In the experiment, we use a relative dielectric constant to train the network LMN without noise, and then uses the trained network to predict the test sample at different noise levels, i.e., 0%, 10%, 15%, 20%. Fig. 4 visualizes the reconstructed relative permittivity distributions of some representative examples. It can be observed that LMN is able to reconstruct the profile with promising results. Relative errors of all the reconstructed permittivity are listed in Table I. It validates the anti-interference ability of LMN in the environment where the scatterer is in strong noise.

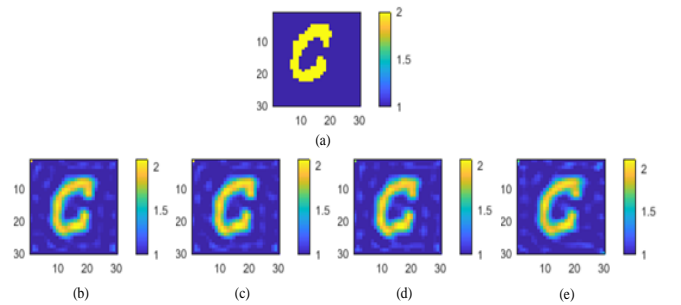


**Fig. 4.** Relative permittivity distribution reconstructions of LMN from scattered fields under various additive white Gaussian noise. (a) Ground truth, (b)(c)(d)(e) reconstruction results under noise level 0%, 10%, 15%, and 20%.

Table I RELATIVE ERRORS  $R_e$  FOR TESTS ON "C" FROM MNIST.

Noise level in scatterer	0%	10%	15%	20%
$R_e$	0.28364	0.28463	0.28596	0.28477

#### 3.3. Comparison under MNIST Database

The effectiveness and superiority of the algorithm is further reflected by comparing the reconstruction results of the two representative methods. i.e., the non-iterative algorithm BA and

iterative algorithm SOM. LMN is inspired from the first-order Born approximation, and the regularization part is replaced by network learning. In Fig. 5, we reconstruct the scatterers from four different SNR scattering fields. From the pattern reconstructed by the same method BA, as the signal-to-noise ratio decreases, the information loss of the reconstructed object gradually increases. However, the pattern change in the reconstruction of SOM and LMN is obviously small. Additionally, both SOM and LMN reconstruct the scatterers better than BA.

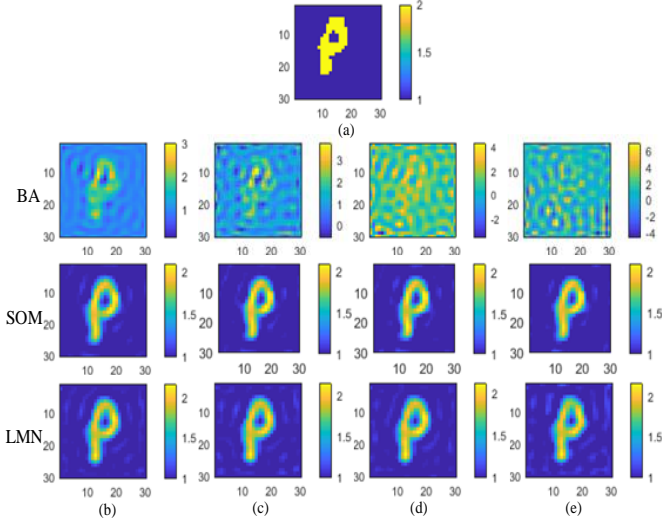


**Fig. 5.** Reconstructed relative permittivity profiles of BA, SOM, LMN from scattered fields under various noise levels. (a) Ground truth, (b)(c)(d)(e) reconstruction results under noise level 0%, 10%, 15%, and 20%.

The above analysis is also reflected in Table II. It shows that BA has certain defects. The proposed scheme can minimize the influence of noise on the reconstructed object due to the CNN denoiser, and has good anti-noise performance. Additionally, by observing and analyzing the reconstructed maps of LMN and SOM, it is found that the image quality of SOM is quite near to that of LMN. Although both reconstruction effects are satisfactory, the iterative time required in SOM is larger. By comparing LMN with SOM, the superiority of the linear algorithm combined with data learning over the non-linear algorithm is demonstrated.

Table II RELATIVE ERRORS  $R_e$  FOR TESTS on “p” from MNIST.

Noise level in scatterer	0%	10%	15%	20%
BA	0.2725	0.3161	0.3575	0.6724
SOM	0.22937	0.23054	0.23381	0.23006
LMN	0.2585	0.2592	0.2588	0.2588

### 3.4. Comparison under “Austria profile”

A more classic scatterer is used to test the performance of the proposed solution. The scatterer consists of a ring and two small circles with the same properties. As shown in Fig. 6, the outer circle radius of the ring is 2 m, and the inner circle radius is 1.5 m. The radius of the small circle is 1 m. The relative dielectric constant of the scatterer is 2. The range of relative permittivity is between 1.1 and 2.0 in the noise-free scattered field.

Fig. 6. visualizes the reconstructed relative permittivity profiles for three methods, where 0% ,10% , 20% and 30%

Gaussian noises are considered in the scattered fields. Since the additive white Gaussian noise in the test procedure may be much higher than that in the training procedure, the case with 30% noise amount is investigated in our experiment.

In the case of 30% noise for the first-order Born approximation, due to the large error, the corresponding inverse scattering reconstruction map is not shown here. Specifically, the trained network with only 0% additive white Gaussian noise is utilized to presented in the training procedure. By observing the reconstruction map, we find that LMN improves the traditional linear method to a certain extent. Although the reconstruction result is only comparable to the non-linear method SOM, LMN uses the same trained network to reconstruct the four different input scattering fields.

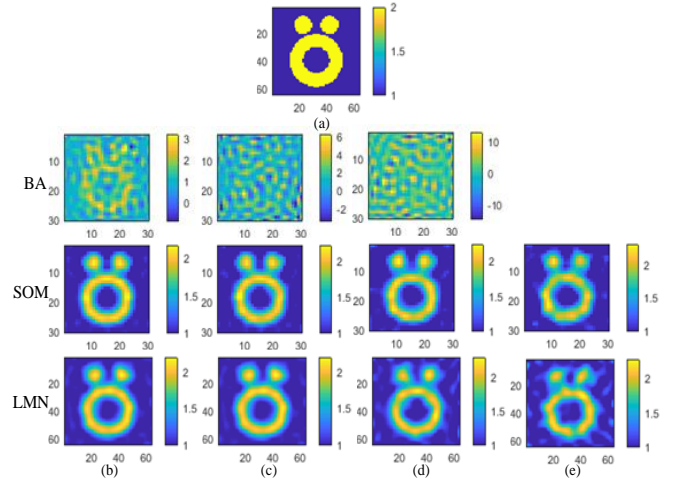


**Fig. 6.** Reconstructed relative permittivity profiles of BA, SOM, LMN from scattered fields under various noise levels. (a) Ground truth, (b)(c)(d)(e) reconstruction results under noise level 0%, 10%, 20%, and 30%.

In Table III, it is found that the relative errors in the reconstruction of the scattered field remain almost unchanged under different noise levels, Therefore, it can be concluded that LMN has a certain anti-interference ability in high noise environment, maintaining good reconstruction effect.

Table III RELATIVE ERRORS  $R_e$  FOR THE TESTS on “Austria profile”.

Noise level in scatterer	0%	10%	20%	30%
BA	0.2077	0.4969	1.3591	NA
SOM	0.13778	0.13883	0.14207	0.14457
LMN	0.14317	0.14398	0.15032	0.16015

## 4. CONCLUSIONS

This work paved a new way to tackle with ISPs via exploiting model-based network learning strategy. By introducing a simple linear model for ISPs, a new model with network-driven regularizer was proposed. For attaining an efficient end-to-end learning, a network architecture and the estimation of hyper-parameters of the network were presented. Experimental results validated its anti-interference ability, i.e., the robustness of the training procedure. Moreover, reconstruction improvement over the traditional linear algorithm to some extent was demonstrated, i.e., it is superior to the classical linear methods and is comparable to the state-of-the-art nonlinear methods.

## REFERENCES

- [1] R. Zoughi, "Microwave non-destructive testing and evaluation principles," Dordrecht, The Netherlands: Springer, 2012.
- [2] R. Persico, "Introduction to ground penetrating radar: Inverse scattering and data processing," Hoboken, NJ, USA: Wiley, 2014.
- [3] A. Quarteroni, L. Formaggia, and A. Veneziani, "Complex systems science in biomedicine," New York, Milan: Springer, 2006.
- [4] R. Chen, Z. Wei, and X. Chen, "Three dimensional through-wall imaging: Inverse scattering problems with an inhomogeneous background medium," in *Proc. IEEE 4th Asia-Pacific Conf. Antennas Propag. (APCAP)*, pp. 505–506, Jul. 2015.
- [5] H. Kagiwada, R. Kalaba, S. Timko, and S. Ueno, "Associate memories for system identification: Inverse problems in remote sensing," *Math. Comput. Model.*, vol. 14, pp. 200–202, Jan. 1990.
- [6] X. Zhuge and A. G. Yarovoy, "A sparse aperture MIMO-SAR-based UWB imaging system for concealed weapon detection," *IEEE Trans. Geosci. Remote Sens.*, vol. 49, no. 1, pp. 509–518, Jan. 2011.
- [7] L. Poli, G. Oliveri, A. Massa, "Microwave imaging within the first-order Born approximation by means of the contrast-field Bayesian compressive sensing," *IEEE Transactions on Antennas and Propagation*, vol. 60, no. 6, pp. 2865–2879, 2012.
- [8] Y. Huang, Q. H. Liu and J. Zhang, "Fast three-dimensional GPR forward and inverse scattering based on wideband diagonal tensor approximation," *Digests of the 2010 14th Biennial IEEE Conference on Electromagnetic Field Computation*, Chicago, IL, pp. 1-1, 2010.
- [9] J.D. Shea, B.D. Van Veen, S.C. Hagness, "A TSVD analysis of microwave inverse scattering for breast imaging," *IEEE Transactions on Biomedical Engineering*, vol. 59, no. 4, pp. 936-945, 2011.
- [10] H. Zhou, Z. Mo, Y. Wang, R. Duan, "Low rank reconstruction algorithm for ground penetrating radar linear inverse imaging," *IET International Radar Conference*, 2015.
- [11] Y. M. Wang and W. C. Chew, "An iterative solution of the twodimensional electromagnetic inverse scattering problem," *Int. J. Imag. Syst. Technol.*, vol. 1, no. 1, pp. 100–108, Jun. 1989.
- [12] W. C. Chew and Y. M. Wang, "Reconstruction of two-dimensional permittivity distribution using the distorted Born iterative method," *IEEE Trans. Med. Imag.*, vol. 9, no. 2, pp. 218–225, Jun. 1990.
- [13] P. M. van den Berg and R. E. Kleinman, "A contrast source inversion method," *Inverse Prob.*, vol. 13, no. 6, p. 1607, Dec. 1997.
- [14] L.-P. Song, C. Yu, and Q. H. Liu, "Through-wall imaging (TWI) by radar: 2-D tomographic results and analyses," *IEEE Trans. Geosci. Remote Sens.*, vol. 43, no. 12, pp. 2793–2798, Dec. 2005.
- [15] X. Chen, "Subspace-based optimization method for solving inversescattering problems," *IEEE Trans. Geosci. Remote Sens.*, vol. 48, no. 1, pp. 42–49, Aug. 2010.
- [16] K. Xu, Y. Zhong, and G. Wang, "A hybrid regularization technique for solving highly nonlinear inverse scattering problems," *IEEE Trans. Microw. Theory Techn.*, vol. 66, no. 1, pp. 11–21, Jan. 2018.
- [17] S. Caorsi and P. Gamba, "Electromagnetic detection of dielectric cylinders by a neural network approach," *IEEE Trans. Geosci. Remote Sens.*, vol. 37, no. 2, pp. 820–827, Mar. 1999.
- [18] L. Li, L. Wang, F. Teixeira, C. Liu, A. Nehorai, and T. Cui, "DeepNIS: Deep neural network for nonlinear electromagnetic inverse scattering," *IEEE Transactions on Antennas and Propagation*, vol. 67, no. 3, pp. 1819-1825, 2019.
- [19] I. T. Rekanos, "Neural-network-based inverse-scattering technique for online microwave medical imaging," *IEEE Trans. Magn.*, vol. 38, no. 2, pp. 1061–1064, Mar. 2002.
- [20] W. Zhun, and X. Chen. "Deep-learning schemes for full-wave nonlinear inverse scattering problems," *IEEE Trans. Geosci. Remote Sens.*, vol. 57, no.4, pp. 1849-1860, 2018.
- [21] H. M. Yao, E. I. Wei, and L. Jiang, "Two-Step Enhanced Deep Learning Approach for Electromagnetic Inverse Scattering Problems," *IEEE Antennas and Wireless Propagation Letters*, vol. 18, no. 11, pp. 2254-2258, 2019.
- [22] W. Zhun, and X. Chen. "Physics-inspired convolutional neural network for solving full-wave inverse scattering problems," *IEEE Transactions on Antennas and Propagation*, vol. 67, no. 9, pp. 6138-6148, 2019.
- [23] H. K. Aggarwal, M. P. Mani and M. Jacob, "MoDL: Model-based deep learning architecture for inverse problems," *IEEE Transactions on Medical Imaging*, vol. 38, no. 2, pp. 394-405, 2019.
- [24] W. H. Press, S. A. Teukolsky, W. T. Vetterling, and B. P. Flannery, "Numerical recipes in C," Cambridge University Press, vol. 1, p. 3, 1988.
- [25] D. P. Kingma and J. L. Ba, "Adam: A method for stochastic optimization," *International Conference on Learning Representations 2015*, pp. 1–15, 2015.
- [26] Y. LeCun, L. Bottou, Y. Bengio, and P. Haffner, "Gradient-based learning applied to document recognition," *Proc. IEEE*, vol. 86, no. 11, pp. 2278–2324, Nov. 1998.